Nanoscale

ROYAL SOCIETY OF CHEMISTRY

PAPER

View Article Online
View Journal | View Issue

Cite this: *Nanoscale*, 2023, **15**, 12270

Superparticles of gold nanorods with controllable bandwidth and spectral shape for lipophilic SERS†

Xun Li,[a] Xi Chen,[a] Jie Liu,[a] Xiaoyu Zhao,[b] Jia Liu,[b] Zhiqun Cheng[a] and Tian-Song Deng *[a]

Received 23rd April 2023,
Accepted 25th June 2023

DOI: 10.1039/d3nr01883k

rsc.li/nanoscale

The plasmonic nanoparticle components assembled by certain methods have great application potential in single particle scattering and surface-enhanced Raman spectroscopy (SERS) detection. Gold nanorods (GNRs) are a type of promising plasmonic material for nanoparticle assembly due to their large, shape-induced local field enhancement and tunable surface plasmon resonances (SPRs). However, it is difficult to obtain the spectra of the anticipated bandwidth and shape, due to the coupling effect between the GNRs and the concentration of GNRs with different SPRs. In this paper, a superparticle assembly method with predictable spectral bandwidth and shape prepared by batch gradient descent (BGD) algorithm fitting and emulsion method is proposed. Specifically, broadband GNRs were obtained by mixing 6 types of GNRs, which the ratios were determined by a BGD algorithm. Then the superparticles were prepared by a method of oil-in-water emulsion with solvent evaporation, resulting in superparticles with broadband spectra from 700 nm to 1100 nm. The bandwidth and shape of the spectra could be tuned by changing the concentration of GNRs of different LSPRs. After removing the CTAB template of mesoporous silica, the assembled broadband superparticles can also measure SERS enhancement for the lipophilic dye molecule Nile red, which opens up a broad space for its sensing application.

Introduction

In the past decades, self-assembly of noble metal nanomaterials has become a research hotspot, and GNRs have attracted much attention due to their unique chemical and physical properties. (i) The adjustable aspect ratio (AR) of the GNRs makes their extinction spectrum highly tunable from visible light to the near-infrared region, (ii) the localized surface plasmon resonance (LSPR) characteristic of the GNRs can enhance the Raman signals of molecules.[1–5] Therefore, they are widely used in optical components,[6–8] SERS,[9–11] sensors,[12–14] catalysis,[15–17] and medical fields.[18–20]

Numerous methodologies have been documented pertaining to the generation of nanoparticle assemblies imbued with plasmonic attributes. Nanoparticle assemblies can be fashioned through bottom-up techniques utilizing molecular connectors,[21,22] or evaporation-driven self-assembly,[23,24] or using top-down approaches such as template-assisted approaches.[25,26] Among these, the simplicity and scalability of the evaporation-driven soft-templated assembly approaches expedite the consolidation of a substantial number of particles and the facile deposition of components on diverse surfaces for localized sensing applications. Naturally, distinctive assembly methods have also yielded certain outcomes. For example, in 2018, Kwon *et al.*[27] synthesized plasma-black colloidal gold superparticles composed of several gold nanospheres using a one-step chemical synthesis method with broadband absorption in the visible and near-infrared regions. However, the bandwidth and shape of the superparticles prepared by this method are unpredictable, and their broadband absorption mainly originates from the mixed solutions. Compared with isotropic gold nanospheres,[28,29] GNRs have extensive anisotropic plasmonic properties, and their plasmonic resonance wavelengths are highly tunable in the visible and near-infrared regions. However, compared with the dispersed GNRs monomers, both theoretic calculations and experimental results show that when the spacing between GNRs decreases, the LSPRs of GNRs are coupled, and the electric field at the gap region increases.[30,31] The coupling effect is related to the concentration and arrangement of GNRs.[32,33]

Gold nanoparticles and their assemblies possess significant applications in SERS detection owing to their substantial localized electric field.[24,34] For example, van der Hoeven *et al.* employed a water-in-oil emulsion coupled with solvent evaporation to drive self-assembly, yielding superparticles exhibiting notable SERS enhancement by adjusting the thickness, poro-

---

[a] *School of Electronics and Information Engineering, Hangzhou Dianzi University, Hangzhou 310018, P. R. China. E-mail: dengts@pku.edu.cn*
[b] *College of Materials and Environmental Engineering, Hangzhou Dianzi University, Hangzhou 310018, P. R. China*

† Electronic supplementary information (ESI) available. See DOI: **https://doi.org/10.1039/d3nr01883k**

sity, and controlled corrosion of mesoporous silica on the surface of GNRs.[23] However, this method is only suitable for testing hydrophilic dye molecules, as hydrophobic dye molecules encounter difficulties in accessing the surface of the GNRs, thereby hindering the SERS signal enhancement effect.

In this study, we obtained the extinction spectra, encompassing the predicted bandwidth and waveform, by fitting the data of mesoporous silica-coated gold nanorods (GNRs@SiO_2) with the BGD algorithm. Additionally, we mixed GNRs@SiO_2 solutions with different LSPRs in accordance with their corresponding weights. This method allows for precise customization of the bandwidth and shape of the anticipated spectrum while establishing an error range to obtain the theoretically optimal spectrum. Subsequently, we employed solvent evaporation of an oil-in-water emulsion to drive self-assembly, resulting in superparticles exhibiting broadband extinction properties within the range of 700–1100 nm. These properties were verified by tests of darkfield single-particle scattering spectroscopy. Moreover, we opened the channel between the lipophilic dye molecule and the GNRs by removing the CTAB template within the mesoporous silica, and obtained oleophilic superparticles with SERS enhancement capabilities.

Experimental

Materials

All chemical materials were used as received without further purification. Hexadecyl-trimethylammonium bromide (CTAB, >99.0%), chloroauric acid ($HAuCl_4 \cdot 4H_2O$), Sodium dodecyl sulfate (SDS), dextrans, Octadecyltrimethoxysilane (OTMS), Cyclohexane (99.50%), Nile red (≥95%), and L-ascorbic acid (AA, >99.99% metals basis) were purchased from Shanghai Macklin Biochemical Technology Co., Ltd. Silver nitrate ($AgNO_3$, >99.8%), sodium oleate (NaOL, >99.88%), Tetraethyl orthosilicate (99.99%), and sodium borohydride ($NaBH_4$, >98%) were purchased from Shanghai Aladdin Biochemical Technology Co., Ltd. Hydrochloric acid (37%) was purchased from Hangzhou Jiachen Chemical Co., Ltd. Methanol (≥99.5%), ethanol (>99.7%), and sodium hydroxide (NaOH, ≥96%), were purchased from Shanghai Gaojing Chemical Co., Ltd. Butylamine was purchased from Sigma-Aldrich Co., Ltd. Ultrapure water with a resistivity of 18.2 MΩ was used in all of the experiments.

GNRs synthesis

The GNRs were synthesized using the method described by Ye *et al.*[35] Preparation of seed solution: 0.25 mL of 0.01 M $HAuCl_4$ solution was added to 10 mL of 0.1 M CTAB solution. Subsequently, 0.6 mL of 0.01 M $NaBH_4$ solution (freshly prepared) at 1200 rpm. After the solution changed from yellow to brown, the stirring was stopped, and the solution was left undisturbed at room temperature for 30 min before use. The preparation of growth solution: in order to prepare the GNRs with an AR = 3.1, 7 g CTAB and 1.23 g NaOL were dispersed into 448 mL deionized water. Then, in sequence, 24 mL 4 mM $AgNO_3$ solution and 25 mL 0.01 M $HAuCl_4$ solution were added in sequence. The solution was stirred at 450 rpm until the color of the solution became colorless. Following that, 1.5 mL of 12.1 M HCl, 1.25 mL of 0.064 M ascorbic acid, and 0.4 mL of seed solution were added sequentially. The total volume of the growth solution was about 500 mL. The growth temperature was set at 30 °C, and the mixture was allowed to grow overnight. GNRs with varying LSPRs were obtained by adjusting the amount of $AgNO_3$, HCl and the seed solution (see Table S1† for details). The prepared GNRs solution was washed twice with ultrapure water at 8000 rpm for 10 min and stored in 100 mL of 1.5 mM CTAB solution.

Fitting spectral data using batch gradient descent

Since the amount of data involved in spectral fitting is relatively small, we used the batch gradient descent algorithm in the gradient descent algorithm based on multiple linear models to fit and predict the GNRs@SiO_2 spectra of different LSPRs. The corresponding weights when the loss function is minimized. The gradient descent algorithm is an iterative algorithm widely used to solve the optimal solution of linear and nonlinear models. Its central idea is to obtain the weight of the time when the loss function is minimized by increasing the number of iterations.

Briefly introduce the principle of the lower gradient descent algorithm. Suppose the multiple linear regression model is:

$$\hat{y} = f(X) = a_0 + a_1x_1 + a_2x_2 + \cdots + a_ix_i + \ldots + a_mx_m = a^{\mathrm{T}}X \tag{1}$$

where $\hat{y}$ is the dependent variable (predicted value), m is the number of explanatory variables, x_i is the ith independent variable, a_j is the jth model coefficient (including the bias a and feature parameter $a_1, a_2, \ldots, a_n$), and a^{T} is the transpose vector of the a_j combination column vector. For the predicted values given by the example $(x^{(1)},y^{(1)})$, $(x^{(2)},y^{(2)})$,…, $(x^{(n)},y^{(n)})$, the mean square error (MSN) is used as the loss function:

$$\mathrm{MSE}(a) = \frac{1}{n}\sum_{i=1}^{n}(a^{\mathrm{T}} \cdot X^{(i)} - y^{(i)})^2 \tag{2}$$

where $y^{(i)}$ (i = 1, 2, …, n) is the value of the sample, $X^{(i)} = (x_1{}^i, x_2{}^i, \ldots, x_n{}^i)^T$, ($i$ = 1, 2, …, n) is the ith feature column vector.

The process of solving the optimal model coefficient through the linear regression model is also the process of training the model (1) to minimize the loss function (2), and the size of this value is used to reflect the degree of fitting of the model, that is, the smaller the loss value, the better the fit.

Calculate the sum of the weights and biases of all training data relative to the gradient of the loss function, that is, get the partial derivative of the loss function MSE(a) with respect to each parameter:

$$\frac{\partial \mathrm{MSE}(a)}{\partial a_j} = \frac{2}{n}\sum_{i=1}^{n}(a^{\mathrm{T}} \cdot X^{(i)} - y^{(i)}) \cdot x_j^{(i)}, \quad j = 1, 2, \ldots, n. \tag{3}$$

Combined with the positive and negative of (3) to judge the relationship between MSE(a) and a, when the result is greater than zero, it means that the relationship between the two is positively proportional. If you want to get the minimized MSE (a), you need to reduce a and substitute it into the next iteration process; conversely, increase a. At the same time, set the step size α (learning rate), and calculate the model parameters for the next iteration by formula (4) until the point with the smallest loss function value is found, namely:

$$a := a - \alpha \cdot \frac{\partial \mathrm{MSE}(a)}{\partial a_j}. \tag{4}$$

After that, the model parameters obtained by iteration are substituted into formula (6) to obtain the next predicted value, which is the iterative process of the gradient descent algorithm.

The batch gradient descent algorithm (BGD) we use improves on the above steps and performs a one-time calculation of eqn (3), namely:

$$\nabla_{\mathrm{a}} \mathrm{MSE}(a) = \left\{ \begin{array}{c} \dfrac{\partial \mathrm{MSE}(a)}{\partial a_0} \\ \cdots \\ \dfrac{\partial \mathrm{MSE}(a)}{\partial a_m} \end{array} \right\} = \frac{2}{n} X^{\mathrm{T}} \cdot (a^{\mathrm{T}} \cdot X - Y). \tag{5}$$

where $Y = (y^{(1)}, y^{(2)}, \ldots, y^{(n)})$ is a column vector consisting of a given true value. Since the number of iterations of the gradient descent algorithm is not easy to determine, we set the tolerance ε. When the amount of change of the loss function is less than ε, the algorithm terminates, and the a_0, a_1, a_2, …, a_n is the weight when the loss function is minimized.

Meso-SiO$_2$ coating

The meso-SiO$_2$ coating were performed following our previous work.[36] In summary, 10 mL of the GNRs dispersed in 1.5 mM CTAB solution was prepared. Then, 0.1 mL of 100 mM NaOH solution was added while stirring at 400 rpm. Subsequently, 30 μL TEOS solution (20 v% in ethanol) was added three times at intervals of 1 h. The reaction was allowed to continue stirring for two days to obtain relatively uniform mesoporous silica with a thickness of about 20 nm. After the reaction, the resulted particles were washed with ultrapure water and ethanol at 8000 rpm for 10 min by centrifugation and then re-dispersed in 10 mL of ethanol.

Removal of CTAB in GNRs@SiO$_2$

To remove the CTAB and open the mesopores of the silica coated GNRs, we washed the GNRs with 0.1 M HCl in ethanol. Specifically, 84 μL HCl (37 wt%, 12.1 M) was added to 10 mL of GNRs@SiO$_2$ stored in ethanol to adjust the pH of the solution to 1. The solution was then sonicated for 2 hours at a power of 400 W (UC-15, ZKI). After sonication, the solution was washed four times with ethanol at 8000 rpm for 10 min and finally dispersed into 1 mL of ethanol.

Surface modification of GNRs@SiO$_2$ by OTMS

Surface modification was carried out following the procedure published by Liu *et al.*[37] First, 1 ml of OTMS, 1 mL of butylamine, and 10 mL of toluene were sequentially added. Then, 1 ml of GNRs@SiO$_2$ with CTAB removed, stored in ethanol, was centrifuged at 8000 rpm for 10 min. The supernatant was removed, and the centrifuged product was added to the mixed solution. And then the mixed solution was sonicated for 3 hours at a power of 400 W (UC-15, ZKI). After the reaction, the mixed solution was washed once with toluene and twice with cyclohexane at 8000 rpm for 10 min, and finally dispersed into 1 mL of cyclohexane.

Self-assembly of superparticles

Self-assembly of water-in-oil was carried out following the procedure published by Mason *et al.*[38] with slight modification. First, 400 mg of dextran and 60 mg of SDS were sequentially added to 10 mL of deionized water. Then, 1 mL of GNRs@SiO$_2$ dispersed in cyclohexane was added. The mixed solution was emulsified by sonicating for 2 min. After that, the oil droplets were naturally volatilized at room temperature. The assembly was completed when the solution changed from milky white to colorless. The lower layer of precipitate was taken out and washed twice with deionized water by centrifugation at 2000 rpm for 10 min. Finally, the obtained superparticles were dispersed into 1 ml of deionized water.

Raman measurements

The Raman measurements were performed using the BX53M microscope of OLYMPUS equipped with an FC-D-785 laser giving 785 nm light, with a maximum power of ≈ 200 mW. The sample preparation process for Raman measurements with superparticles was shown in Fig. 5a. First, superparticles were dropped onto a piece of silicon and allowed to evaporate naturally. Next, 10 μL of Nile red in the toluene of 10 μg analyte per g solvent concentration was dropped. After drying again, an empty copper grid was placed on top of the wafer and fixed with a conductive adhesive. The Raman measurements were performed by a 785 nm laser with a power of 200 mW, 50× air objective (NA = 0.75), 10 s exposure time and 1 accumulation per spot.

Single particle scattering measurements

Single-particle dark-field scattering measurements were conducted using an Olympus BX53M optical microscope, which was integrated with a halogen lamp (100 W) and a spectrometer model NOVA 2S-EX (325–1100 nm). A dark-field objective (100×, numerical aperture = 0.80) was employed for both exciting the particles with white light and collecting the scattered light. The scattered light was reflected to the entrance slit of the monochromator. The scattering spectra from the individual particles were corrected by subtracting the background spectra taken from the adjacent regions without particles and dividing with the pre-calibrated response curve of the entire optical system.

FDTD simulations

The FDTD method is an explicit time-marching algorithm used to solve Maxwell's curl equations on a discretized spatial grid. The FDTD simulations were carried out with a commercial software, FDTD Solutions 8.19.1584 (Lumerical Solutions). A light pulse in the wavelength range of 300–1400 nm was launched into a box containing GNRs to simulate a propagating plane light wave interacting with the nanorod. The GNRs were surrounded by a virtual boundary with an appropriate size. The GNRs and its surrounding medium inside the boundary were divided into meshes of 1 nm in size. The sizes of the GNRs were taken from their average values. The thickness of the mesoporous silica shell is uniformly taken at 20 nm. The refractive indices of the surrounding air and water were set to be 1.0 and 1.33, respectively.

Characterizations

Optical extinction spectra were recorded with a UV-1900i (190–1100 nm) Spectrophotometer (Shimadzu, Japan) with a 10 mm optical path. Transmission electron-microscopy (TEM) images were obtained with a HT-7700 microscope (Hitachi, Japan) operating at 100 kV. Size parameters of GNRs were estimated from analysis of TEM images (40 000×) on ImageJ software. SEM imaging was performed on a JEOL JSM6460LV microscope operating at 3 kV.

Results and discussion

In this study, we self-assembled GNRs to obtain superparticles with controlled spectral bandwidth and shape. Fig. 1 illustrates the schematic of the entire experimental procedure. Firstly, six types of GNRs with different LSPRs were coated with mesoporous silica and mixed in a specific proportion to obtain a broadband extinction system (Fig. 1a–c). Then, the superparticles with broadband extinction properties were obtained (Fig. 1c–f) through the oil-in-water emulsion method. This process involved three main steps: surface modification with lipophilic octadecyltrimethoxysilane (OTMS) molecules, emulsification of oil droplets in water, and slow solvent evaporation.

Design of GNRs@SiO$_2$ with broadband extinction spectra

GNRs with different ARs have different extinction peaks due to their longitudinal LSPRs. In order to obtain a system with a broadband extinction band, we prepared six types of GNRs with different ARs by "seed-mediated" growth method[35] (Table S1,† see the Method section for details). Among them, the normalized spectra and TEM images of the GNRs are shown in Fig. 2a (1–6) and Fig. 2b, respectively. The actual solution dispersion and measured spectra are shown in Fig. S1 (a and b).† When the distance between GNRs is less than 10 nm, a strong coupling effect occurs between them, leading to changes in their absorption and scattering characteristics.[39,40] Coating mesoporous silica on the surface of GNRs can effectively control the spacing between GNR monomers, thereby reducing the coupling effect. The spectrum of GNRs@SiO$_2$ is only slightly redshifted due to the change in refractive index.[36,41] Therefore, using GNRs@SiO$_2$

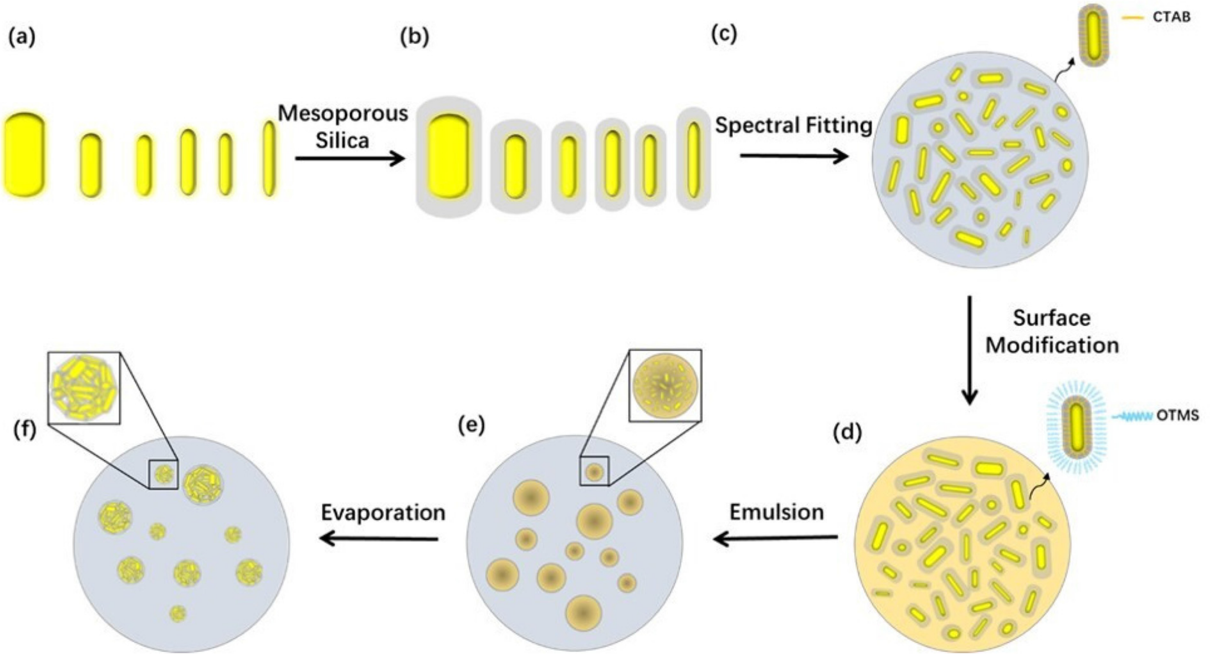

Fig. 1 Schematic diagram of the preparation of superparticles with controllable bandwidth and spectral shape. (a) GNRs with 6 different LSPRs, ranging from 680 nm to 1090 nm. (b) Coating of GNRs with mesoporous silica. (c) The spectra of GNRs@SiO$_2$ with 6 different LSPRs were fitted using the BGD algorithm, and then mixed according to the calculated weights. (d) Surface modification of the mixed GNRs@SiO$_2$ with lipophilic OTMS. (e) Mixing of GNRs@SiO$_2$ dispersed in cyclohexane with a certain amount of water/SDS/dextran, followed by sonication to obtain an oil-in-water emulsion. (f) Self-assembly driven by the evaporation of the oil phase to obtain broadband superparticles.

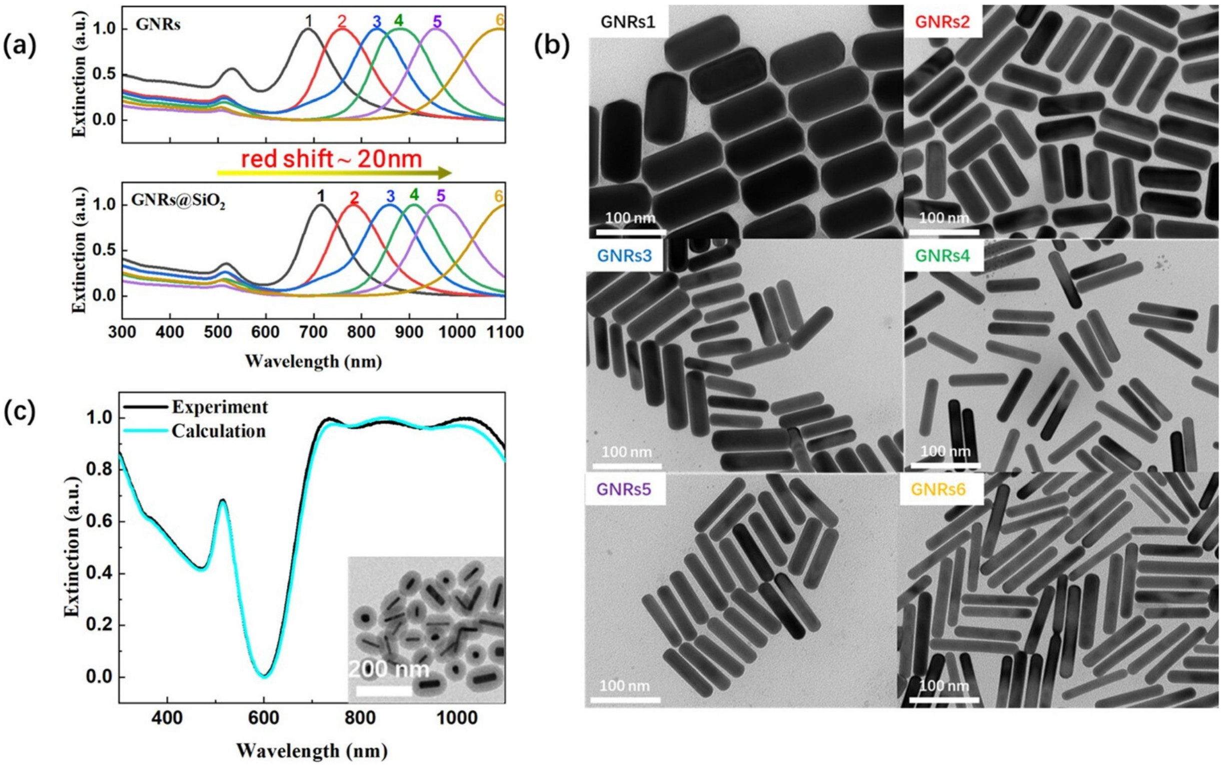

Fig. 2 Extinction spectroscopy and TEM characterization. (a) Extinction spectra of GNRs 1–6 with LSPRs at 680, 760, 830, 880, 950, 1090 nm, and GNRs@SiO$_2$ with LSPRs at 716, 784, 860, 910, 966, >1100 nm. (b) TEM images corresponding to GNRs 1–6 with different LSPRs in (a). (c) The BGD algorithm was used to fit the spectra of GNRs@SiO$_2$ 1–6 with different LSPRs, resulting in spectra with a broad bandwidth. The inset in (c) shows a TEM image of the mixed GNRs@SiO$_2$.

for controllable modulation of extinction or scattering spectra is an effective approach. We coated the surface of the GNRs with a layer of mesoporous silica with 20 nm thickness to increase the spacing between the GNRs.[36] As a result, the extinction spectra of GNRs@SiO$_2$ in the ethanol solution exhibited a redshift of approximately 20 nm compared to GNRs in the water solution. The actual solution color and measured spectra are shown in Fig. S1(c and d).† TEM images corresponding to GNRs@SiO$_2$ 1–6 with different LSPRs are shown in Fig. S2.† We also did finite difference time domain (FDTD) simulations for GNRs and GNRS@SiO$_2$, and the obtained extinction spectra are shown in Fig. S3.† The simulated spectra and experimental results are generally consistent. Compared to the simulated spectra, the experimental results are a little broadening and slight shift in the peak position due to the polydispersity of the GNRs. Furthermore, the electric field distribution of the GNRs is shown in Fig. S4,† with a strong localized field observed at the tips of the GNRs. After coating with a 20 nm silica shell, the electric field on the surface of silica shell is significantly weakened (Fig. S5†), confirming the weak plasmonic coupling between GNRs@SiO$_2$.

According to Lambert-Beer's law, the absorbance is proportional to the concentration of a substance within a certain absorbance range. Therefore, we employed the linear regression equation of the BGD algorithm and six types of GNRs@SiO$_2$ with different LSPRs as the original data to fit the spectra in the 700–1100 nm range with an intensity of 1. Since the number of iterations of the gradient descent algorithm is not easy to determine, we set a tolerance value ε. The algorithm terminates when the change of the loss function is less than ε, and the corresponding weights are minimized. The controllable bandwidth is mainly achieved through the tunability of GNRs, which allows for extinction from visible light to near-infrared.[32,40] Fig. 2c displays the measured and calculated spectra dispersed in an ethanol solution, demonstrating good agreement between the experimental and calculated results. As a control test, when we simply mixed the 6 types of GNRs@SiO$_2$ in equal volume ratios (1 : 1 : 1 : 1 : 1 : 1), the resulting spectra (Fig. S6†) did not exhibit the desired broadband characteristics. Therefore, without the BGD algorithm fitting process, spectra with customized bandwidths and shapes cannot be obtained.

Self-assembly of GNRs@SiO$_2$ into broadband superparticles

The self-assembly of the GNRs@SiO$_2$ with broadband extinction properties was achieved through the solvent evaporation method of oil-in-water emulsion, resulting in the formation of lipophilic superparticles suitable for molecular sensing of lipophilic dyes. Since GNRs@SiO$_2$ disperses well in ethanol (Fig. S7a†) but poorly dispersed in oily solvents, we modified the surface of GNRs@SiO_2 with a lipophilic OTMS molecular layer. Fig. S7b† demonstrates the oil–water layering, indicating that the modified particles can disperse well in the upper layer of the oily solvent. To emulsify GNRs@SiO_2@OTMS in a cyclohexane (about 5 vol% in H_2O) aqueous dispersion, dextran and SDS were added, followed by ultrasonic for 2 min (Fig. S7c†). Fig. S8† shows the cyclohexane oil droplets in the corresponding emulsion. The size distribution of the oil droplets in the emulsion is broad, resulting in different sizes of the superparticles obtained by subsequent drying of the oil droplets (Fig. S7d†).

In general, the self-assembled spherical superparticles exhibit similar spectra in solution compared to the mixed GNRs@SiO_2 broadband systems. It can be observed that both the spectra of the solution before and after self-assembly show an extinction band at 700–1100 nm (Fig. 3a), which confirms the anticipated negligible coupling effect between GNRs@SiO_2 nanoparticles. The spectra of superparticles are the results of the linear superposition of each GNR sample. This is consistent with our initial expectations of superparticles with adjustable bandwidth and shape. Fig. 3b presents a typical TEM image of the broadband superparticles with an average size of 1.6 μm.

As a control experiment, we have prepared superparticles composed of only one type of GNRs@SiO_2 with an LSPR at 784 nm (Fig. S9a†). It can be observed that upon the assembly of large-sized superparticles, despite the surface being coated with a mesoporous silica shell of about 20 nm, some coupling between particles occurs, resulting in a slight broadening of the spectral bandwidth.[23] Fig. S9b† shows a TEM image of the narrowband superparticles with an average size of 1.1 μm.

By testing dark field single-particle scattering of broadband superparticles, the scattering spectrum of a single superparticle is also in the range of 700–1100 nm (Fig. 3c). Prior to the dark field single-particle scattering test of superparticles, we verified the accuracy of the set-up by using single-particle scattering data from GNRs@SiO_2 samples with known spectra. When the diameter of the GNRs is larger, the ratio of scatter-

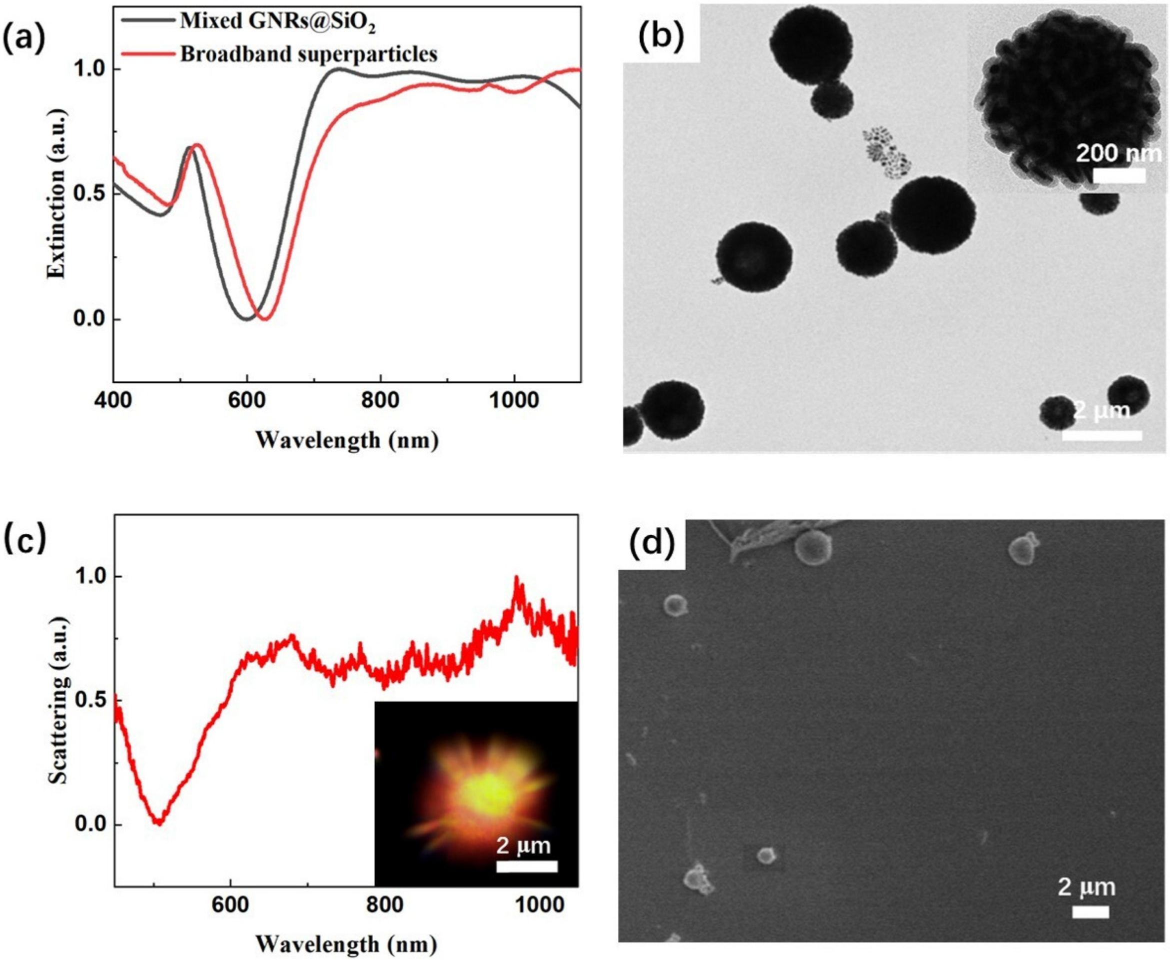

Fig. 3 Extinction spectroscopy and single-particle scattering spectra of superparticles. (a) Extinction spectroscopy of mixed GNRs@SiO_2 and broadband superparticles. (b) TEM image of superparticles with an average size of 1.6 μm. (c) Single-particle scattering spectra of a broadband superparticle. The inset shows a picture of the tested particles taken in the dark field. (d) SEM image of superparticles used for single-particle scattering measurement.

ing to absorption cross-section is greater.[42] Therefore, we chose Fig. 2a1 to prepare samples on silicon wafers for single-particle scattering tests, and the results are shown in Fig. S10.† Fig. S10a† shows the particle distribution of the GNRs@SiO_2 photographed under the optical microscope. It can be observed that the distance between the particles is much larger than the particle size, thus the interaction between superparticles could be neglected. Fig. S10b† displays the single-particle scattering spectrum of the treated GNRs@SiO_2, and its overall spectrum exhibits a certain blue shift relative to the spectrum in aqueous solution due to the change of the refractive index of the medium.[42]

On the basis of testing GNRs single-particle scattering, we conducted single-particle scattering measurements on broadband superparticles. Fig. 3c shows the single-particle scattering spectrum of the GNRs@SiO_2 superparticle, and it exhibits a good broadband characteristic in the range of 700–1100 nm. Fig. 3d displays the particle distribution of the broadband superparticles photographed under the SEM, revealing that the distance between the particles is significantly larger than the particle size, indicating negligible interaction between superparticles. Fig. S11† presents additional single-particle scattering spectra of broadband superparticles along with their corresponding photographs. Similarly, due to the change in the refractive index of the medium, the overall spectrum has a certain blue shift about 70 nm compared to the spectrum in the aqueous solution shown in Fig. 3a.[42] These results confirm the hypothesis that the superparticles possess the anticipated bandwidth and shape.

The coupling effect between the GNRs@SiO_2 particles of the superparticles obtained by our self-assembly method only affects the full width at half maximum (FWHM) of the extinction spectra, making it wider, but does not change the peak position corresponding to the longitudinal LSPR peak. This is despite the fact that the thickness of the coated mesoporous silica reaches about 20 nm, and the distance between the GNRs is at least twice of the shell thickness. In any case, from the spectra of the narrowband superparticles (Fig. S9a†), it is evident that there is still a coupling effect between the GNRs. Therefore, we conducted FDTD simulations of the GNRs@SiO_2 with different arrangements, considering the polarization direction of the incident light along the longitudinal axis of the rod. Among them, Fig. 4(a–d) presents the extinction spectra of the GNRs@SiO_2 in different arrangements, while Fig. 4(e–h) illustrates the corresponding electric field distribution.

The side-by-side arrangement leads to a blueshift of the extinction spectra (Fig. 4b), while head-to-head arrangement leads to redshift of the extinction spectra (Fig. 4c). Considering the effect of coupling, the side-by-side arrangement is equivalent to reducing the overall AR, while the head-to-head arrangement is equivalent to increasing the overall AR.[43] When these two arrangements are combined (Fig. 4d), the peak position corresponding to the longitudinal axis peak in the extinction spectra is nearly the same as that of a single GNRs@SiO_2, indicating that the influence of weak coupling between GNRs@SiO_2 on peak position cancels out due to the randomness of the arrangement. Compared to the bandwidth of the single GNRs@SiO_2 (Fig. 4a), the FWHM changes from 120 nm to 180 nm in Fig. 4d, which also explains the increase in bandwidth after assembling narrowband superparticles in Fig. S9a.† In addition, we performed a similar FDTD simu-

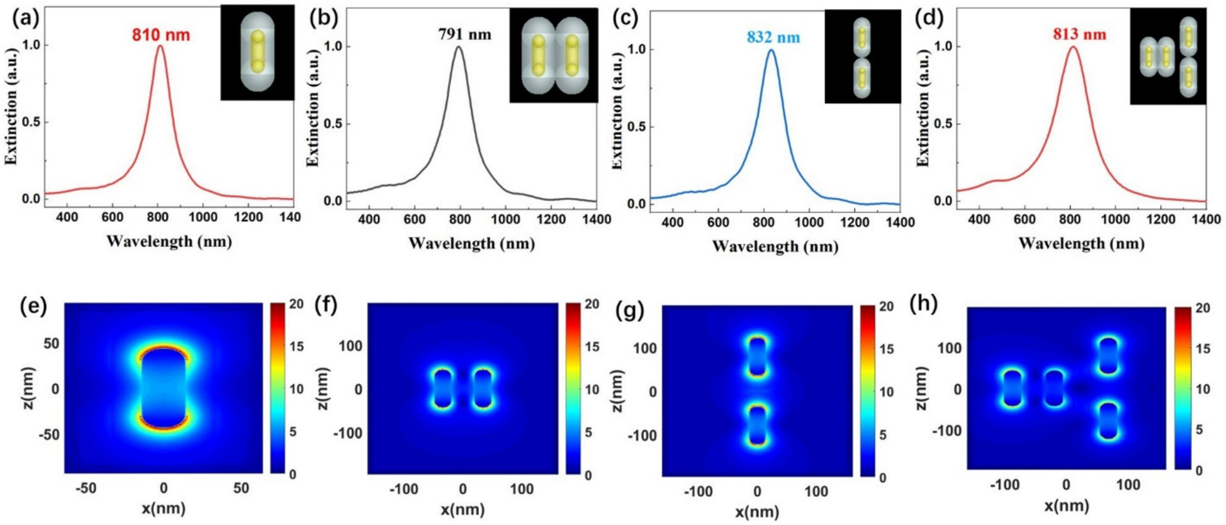

Fig. 4 The extinction spectra and electric field distributions obtained by FDTD simulations illustrate that the plasmonic coupling effect between the GNRs@SiO_2 can be ignored. (a and e) Extinction spectra (a) and electric field distribution (e) of the GNRs@SiO_2 with the LSPR at 810 nm (as shown in Fig. S3b†). (b and f) (b) depicts two GNRs@SiO_2 of the same size as the model in (a) arranged side-by-side and (f) shows the corresponding electric field distribution. (c and g) (c) represents two GNRs@SiO_2 of the same size as the model in (a) arranged head-to-head, and (g) displays the corresponding electric field distribution. (d and h) (d) demonstrates the GNRs@SiO_2 arranged side-by-side and head-to-head together, with a peak position similar to that of (a), and (h) is the electric field distribution.

lation (Fig. S12†) using a GNRs@SiO$_2$ of another size and obtained similar results. Comparing the spectra of Fig. S12a and Fig. S12d,† the peak positions of LSPRs are almost the same, while the corresponding FWHM values are 115 nm and 160 nm respectively. In general, when the spacing between GNRs@SiO$_2$ is small enough, they will affect each other. However, in a random system with a sufficient number of samples, the overall effect of this interaction only results in an increased FWHM without affecting the peak position of the spectra. This partly explains the broadband scattering effect of individual superparticles within the bandwidth of 700–1100 nm.

Superparticles with SERS performance

On the basis of the method used to prepare broadband superparticle, we further prepared superparticles with lipophilic dye molecules and controllable bandwidth by removing the CTAB template from the GNRs@SiO$_2$. To remove the CTAB template from the mesopores of the GNRs coated with mesoporous silica, we washed them with an acidified ethanol solution (0.10 M hydrochloric acid). This process opened up channels for the dye molecules to come into contact with the GNRs.[44] We investigated the SERS-enhancing effect of Nile red dye molecules before and after removal of the CTAB in the GNRs@SiO$_2$ (Fig. S13†). Among them, the Raman signal was nearly undetectable in the GNRs@SiO$_2$ without removing the CTAB template, but a significant Raman characteristic peak at 590 cm^{-1} appeared after the removal of the CTAB template. To facilitate SERS testing and SEM characterization, we employed a combined SERS-SEM method, as illustrated in Fig. 5a. The superparticles were drop-casted on a silicon wafer, dried, and exposed to a toluene solution containing 10 μg of Nile red analyte per g. After drying, a TEM detection grid was placed on top and fixed with conductive glue. We chose to use Nile red dye for this experiment due to its lipophilic properties and distinct characteristic Raman peak at 590 cm^{-1}.[45] Furthermore, since the surface of the GNRs@SiO$_2$ was modified with lipophilic OTMS molecules, the dye molecules could easily go through the mesopores SiO$_2$ shell.

Fig. 5(b–d) shows the SERS-enhanced effect of different particles on Nile red dye molecules, as measured by the SERS-SEM method, along with the corresponding SEM images. The results of Fig. 5b confirm that the superparticles, after removing the CTAB template, exhibit a significant SERS-enhancing effect on

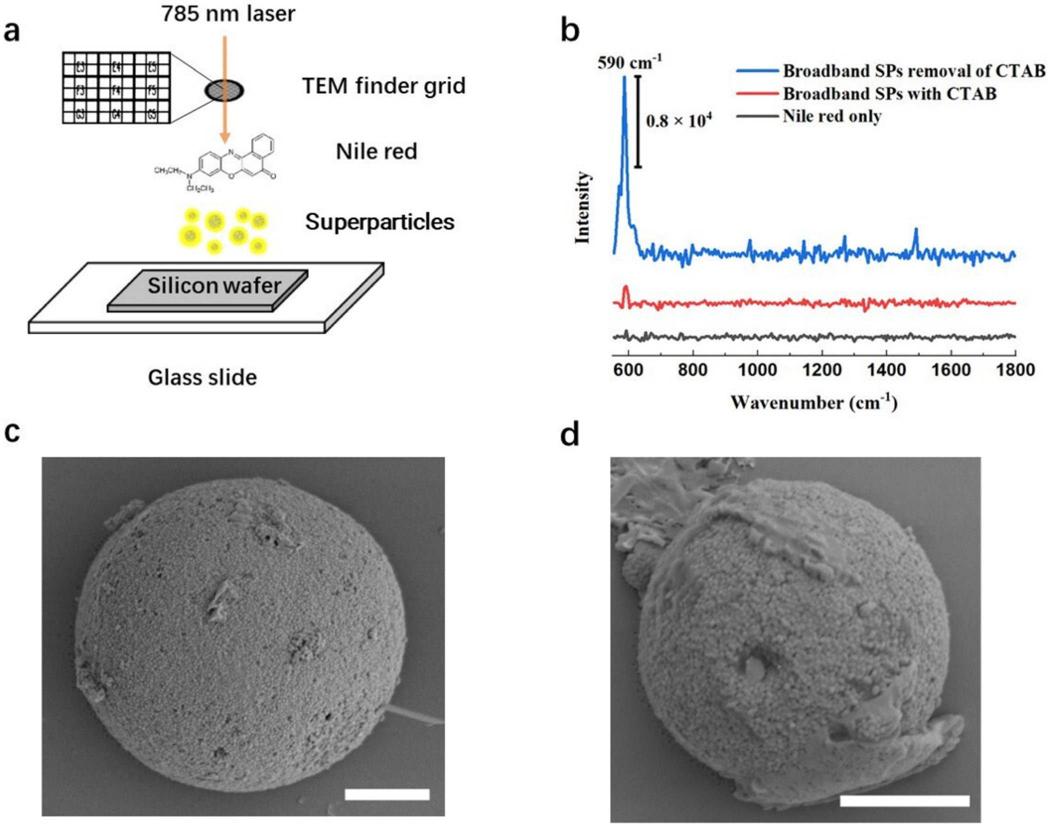

Fig. 5 SERS and corresponding SEM characterization of superparticles. (a) Schematic overview of the sample preparation for the Raman measurements. (b) The dye is Nile red dispersed in toluene. The black is the result of SERS spectrum with Nile red only. The red and blue curves correspond to the SERS enhancement effect of superparticles with CTAB and removal of CTAB, respectively. The Raman scattering peak intensity of the red curve at 590 cm^{-1} is about 0.5 × 10^3. (c and d) SEM images of superparticles with CTAB and removal of CTAB (d), which were measured SERS spectra in (b). Scale bars represent 2 μm.

Nile red dye molecules. The enhancement factor (EF) for superparticles was quantified using the following relation:[23]

$$\mathrm{EF}=\frac{I_{\mathrm{S}}}{I_{\mathrm{R}}}\cdot\frac{N_{\mathrm{R}}}{N_{\mathrm{s}}} \tag{6}$$

where I_S and I_R are the intensity at 590 cm^{-1} in the surface-enhanced spectrum and the Raman spectrum, respectively, and N_s and N_R are the concentration of analyte molecule sampled for SERS and Raman spectra, respectively. The EF was in the range of 10^4 for superparticles removal of CTAB, and approximately 16 times larger than that of the superparticles with CTAB. Fig. 5c and d are the corresponding SEM of superparticles prepared without removal of the CTAB template and removal of the CTAB template in Fig. 5b, respectively. In Fig. S14,† we present Raman spectra of broadband superparticles with different sizes and positions, demonstrating the reproducibility of our prepared superparticles for SERS testing of Nile red dye molecules. Furthermore, based on the Raman spectra in Fig. S14,† the observed intensities of characteristic peaks do not exhibit a clear correlation with the size of the superparticles. This observation can be explained by our sample preparation method. We performed drop casting of dye molecules onto the sample followed by drying, leading to non-uniform distribution of dye molecules on the sample surface due to the coffee ring effect. Consequently, it's lack of a clear correlation between the measured Raman spectra's characteristic peak intensities and the size of the superparticles. These results further validate the universality of the SERS-enhancing effect of the superparticles prepared after removing the CTAB template in the GNRs@SiO_2. In general, by removing the CTAB template in the GNRs@SiO_2, we successfully prepared superparticles that exhibit a SERS-enhancing effect on lipophilic dye molecules, in addition to possessing adjustable bandwidth and shape.

Conclusions

In summary, we have designed GNRs@SiO_2 with broadband extinction characteristics. The bandwidth and shape of the extinction spectra of GNRs@SiO_2 can be adjusted by varying the proportion of particles with different LSPRs. On this basis, we successfully self-assembled superparticles through solvent evaporation in an oil-in-water emulsion. The resulting superparticles exhibit the same broadband extinction properties as the GNRs@SiO_2. In addition, we obtained superparticles with a pronounced SERS effect on lipophilic dyes by removing the CTAB template. This method allows us to obtain superparticles with desired bandwidth and shape in their extinction spectra, while disregarding the plasmonic coupling effect between GNRs@SiO_2 particles. The assembly process employed in our study, based on the evaporation-driven self-assembly method using a soft-template, is simple and scalable. The component size of the superparticles can be adjusted down to the micron scale, enabling their easy deposition on various surfaces. This makes them suitable for localized sensing tests of lipophilic substances. It is foreseeable that these customizable superparticles with specific spectral bandwidth and shape hold great potential for a wide range of applications in various fields.

Conflicts of interest

There are no conflicts to declare.

Acknowledgements

The authors thank Sudan Shen for her assistance in TEM at State Key Laboratory of Chemical Engineering (Zhejiang University). The authors also acknowledge financial support from National Natural Science Foundation of China (NSFC, Grant No. 61905056). This work was also supported by National Key R&D Program of China (Grant: 2018YFE0207500), the National Natural Science Foundation (Grant 91938201 and 61871169), Zhejiang Provincial Natural Science Foundation (Grant LZ20F010004) and Project of Ministry of Science and Technology (Grant D20011).

References

1 H. Chen, L. Shao, Q. Li and J. Wang, *Chem. Soc. Rev.*, 2013, **42**, 2679–2724.
2 A. Sanchez-Iglesias, N. Winckelmans, T. Altantzis, S. Bals, M. Grzelczak and L. M. Liz-Marzan, *J. Am. Chem. Soc.*, 2017, **139**, 107–110.
3 J. J. Li, T. Li, J. Zhu and J. W. Zhao, *Plasmonics*, 2018, **13**, 1433–1439.
4 S.-Y. Ding, J. Yi, J.-F. Li, B. Ren, D.-Y. Wu, R. Panneerselvam and Z.-Q. Tian, *Nat. Rev. Mater.*, 2016, **1**, 16021.
5 A. M. Gabudean, D. Biro and S. Astilean, *J. Mol. Struct.*, 2011, **993**, 420–424.
6 J. Lee, J. Koo, J. Lee and J. H. Lee, *J. Lightwave Technol.*, 2016, **34**, 5250–5257.
7 K. Cai, W. Y. K. Cai, W. Y. Zhang, J. Zhang, H. Q. Li, H. Y. Han and T. Y. Zhai, *ACS Appl. Mater. Interfaces*, 2018, **10**, 36703–36710.
8 L. D. Yue, C. Sun, Q. Cheng, Y. F. Ding, J. W. Wei and R. B. Wang, *Chem. Commun.*, 2019, **55**, 13506–13509.
9 X. Y. Peng, D. Li, Y. T. Li, H. B. Xing and W. Deng, *J. Mater. Chem. B*, 2021, **9**, 1123–1130.
10 R. Moldovan, V. Toma, B. C. Iacob, R. I. Stiufiuc and E. Bodoki, *Sensors*, 2022, **22**, 236.
11 C. Y. Zhang, L. J. Huang, D. W. Sun and H. B. Pu, *J. Hazard. Mater.*, 2022, **426**, 127824.
12 L. Susu, A. Campu, A. M. Craciun, A. Vulpoi, S. Astilean and M. Focsan, *Sensors*, 2018, **18**, 3035.
13 X. Han, J. K. Tian, Z. W. Li, T. G. Wu, G. M. Ji, S. L. Li, F. Xing and Y. H. Zhang, *Appl. Surf. Sci.*, 2022, **587**, 152873.
14 D. Pratap, Vikas, R. Gautam, A. K. Shaw and S. Soni, *Colloids Surf. A*, 2022, **635**, 128054.
15 Y. Mu, H. Zhang, W. Zheng and X. Cui, *New J. Chem.*, 2017, **41**, 786–792.

16 J. E. S. van der Hoeven, J. Jelic, L. A. Olthof, G. Totarella, R. J. A. van Dijk-Moes, J. M. Krafft, C. Louis, F. Studt, A. van Blaaderen and P. E. de Jongh, *Nat. Mater.*, 2021, **20**, 1216–1220.
17 Z. Yong, Q. Shi, R. Fu and W. Cheng, *Adv. Mater. Interfaces*, 2020, **8**, 2001686.
18 H. Yang, H. P. He, Z. R. Tong, H. B. Xia, Z. W. Mao and C. Y. Gao, *J. Colloid Interface Sci.*, 2020, **565**, 186–196.
19 H. J. Shan, X. F. Zhou, B. Tian, C. Y. Zhou, X. Gao, C. W. Bai, B. C. Shan, Y. Z. Zhang, S. X. Sun, D. D. Sun, Q. Fan, X. Z. Zhou, C. Wang and J. Y. Bai, *Biomaterials*, 2022, **284**, 121482.
20 Z. Wei, J. Sun, S. Lu, Y. W. Liu, B. Wang, L. Zhao, Z. L. Wang, K. Liu, J. J. Li, J. J. Su, F. Wang, H. J. Zhang and Y. Yang, *Adv. Mater.*, 2022, **34**, 2110062.
21 L. Song, N. Qiu, Y. Huang, Q. Cheng, Y. Yang, H. Lin, F. Su and T. Chen, *Adv. Opt. Mater.*, 2020, **8**, 1902082.
22 X. Yue, X. J. Liu, N. Yan and W. Jiang, *J. Phys. Chem. C*, 2020, **124**, 20458–20468.
23 J. E. S. Hoeven, H. Gurunarayanan, M. Bransen, D. A. M. Winter, P. E. Jongh and A. Blaaderen, *Adv. Funct. Mater.*, 2022, **32**, 2200148.
24 Y. Liu, Y. Zhang, H. Ding, S. Xu, M. Li, F. Kong, Y. Luo and G. Li, *J. Mater. Chem. A*, 2013, **1**, 3362–3371.
25 M. T. Gole, Z. W. Yin, M. C. Wang, W. N. Lin, Z. R. Zhou, J. Leem, S. Takekuma, C. J. Murphy and S. Nam, *Sci. Rep.*, 2021, **11**, 12232.
26 K. Sivashanmugan, J. D. Liao, J. W. You and C. L. Wu, *Sens. Actuators, B*, 2013, **181**, 361–367.
27 N. Kwon, H. Oh, R. Kim, A. Sinha, J. Kim, J. Shin, J. W. M. Chon and B. Lim, *Nano Lett.*, 2018, **18**, 5927–5932.
28 Y. Q. Zheng, X. L. Zhong, Z. Y. Li and Y. N. Xia, *Part. Part. Syst. Charact.*, 2014, **31**, 266–273.
29 Q. F. Ruan, L. Shao, Y. W. Shu, J. F. Wang and H. K. Wu, *Adv. Opt. Mater.*, 2014, **2**, 65–73.
30 P. Pramod and K. G. Thomas, *Adv. Mater.*, 2008, **20**, 4300–4305.
31 R. C. Ferrier, H. S. Lee, M. J. A. Hore, M. Caporizzo, D. M. Eckmann and R. J. Composto, *Langmuir*, 2014, **30**, 1906–1914.
32 C. Fernandez-Lopez, L. Polavarapu, D. M. Solis, J. M. Taboada, F. Obelleiro, R. Contreras-Caceres, I. Pastoriza-Santos and J. Perez-Juste, *ACS Appl. Mater. Interfaces*, 2015, **7**, 12530–12538.
33 A. M. Funston, C. Novo, T. J. Davis and P. Mulvaney, *Nano Lett.*, 2009, **9**, 1651–1658.
34 J. Qian, L. Jiang, F. H. Cai, D. Wang and S. L. He, *Biomaterials*, 2011, **32**, 1601–1610.
35 X. Ye, C. Zheng, J. Chen, Y. Gao and C. B. Murray, *Nano Lett.*, 2013, **13**, 765–771.
36 T.-S. Deng, J. E. S. van der Hoeven, A. O. Yalcin, H. W. Zandbergen, M. A. van Huis and A. van Blaaderen, *Chem. Mater.*, 2015, **27**, 7196–7203.
37 B. Liu, T. H. Besseling, M. Hermes, A. F. Demirors, A. Imhof and A. van Blaaderen, *Nat. Commun.*, 2014, **5**, 3092.
38 T. G. Mason and J. Bibette, *Langmuir*, 1997, **13**, 4600–4613.
39 M. Shanthil, R. Thomas, R. S. Swathi and K. G. Thomas, *J. Phys. Chem. Lett.*, 2012, **3**, 1459–1464.
40 H. Xiang, Z. Hu, C. Xin, H. J. Lin, L. Aigouy, Z. Chen, L. Zhou and X. Yuan, *Adv. Mater. Technol.*, 2021, **7**, 2101217.
41 V. Pellas, J. Blanchard, C. Guibert, J. M. Krafft, A. Miche, M. Salmain and S. Boujday, *ACS Appl. Nano Mater.*, 2021, **4**, 9842–9854.
42 W. H. Ni, X. Kou, Z. Yang and J. F. Wang, *ACS Nano*, 2008, **2**, 677–686.
43 L. S. Slaughter, Y. P. Wu, B. A. Willingham, P. Nordlander and S. Link, *ACS Nano*, 2010, **4**, 4657–4666.
44 J. E. S. van der Hoeven, T. S. Deng, W. Albrecht, L. A. Olthof, M. A. van Huis, P. E. de Jongh and A. van Blaaderen, *ACS Omega*, 2021, **6**, 7034–7046.
45 J. A. Kraai, A. X. Wang and G. L. Rorrer, *Adv. Mater. Interfaces*, 2020, **7**, 2000191.

Supporting information:

Superparticles of gold nanorods with controllable bandwidth and spectral shape for lipophilic SERS

Xun Li[†], *Xi Chen*[†], *Jie Liu*[†], *Xiaoyu Zhao*[‡], *Jia Liu*[‡], *Zhiqun Cheng*[†], *Tian-Song Deng*[†,*]

[*] *Corresponding author. E-mail: dengts@pku.edu.cn*

[†]School of Electronics and Information Engineering, Hangzhou Dianzi University, Hangzhou 310018, P. R. China.

[‡]College of Materials and Environmental Engineering, Hangzhou Dianzi University, Hangzhou 310018, P. R. China.

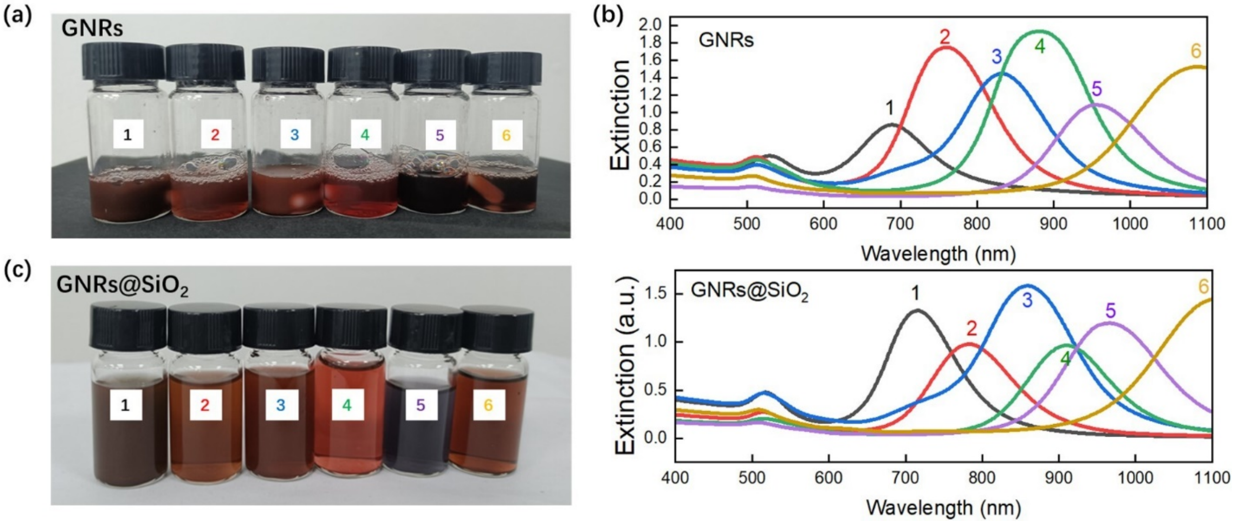

Fig. S1 Photographs and spectra of different GNRs and GNRs@SiO$_2$. (a) The prepared GNRs with six different LSPRs were dispersed in 1.5 mM CTAB, corresponding to Fig. 2a (1-6) of GNRs. (b) Measured spectra of the samples corresponding to GNRs in (a). (c) Six GNRs of different LSPRs were dispersed in ethanol solution after coating a mesoporous silica shell, corresponding to Fig. 2a (1-6) of GNRs@SiO$_2$. (d) Measured spectra of the samples corresponding to GNRs@SiO$_2$ in (c).

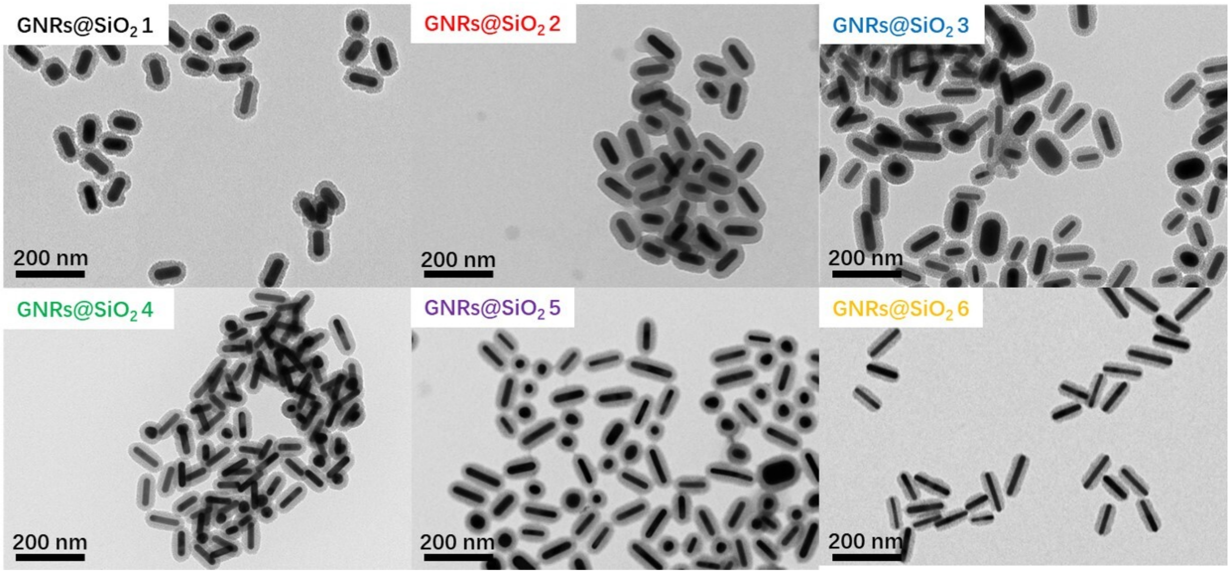

Fig. S2 TEM images corresponding to GNRs@SiO_2 1-6 with different LSPRs in Fig. 2a.

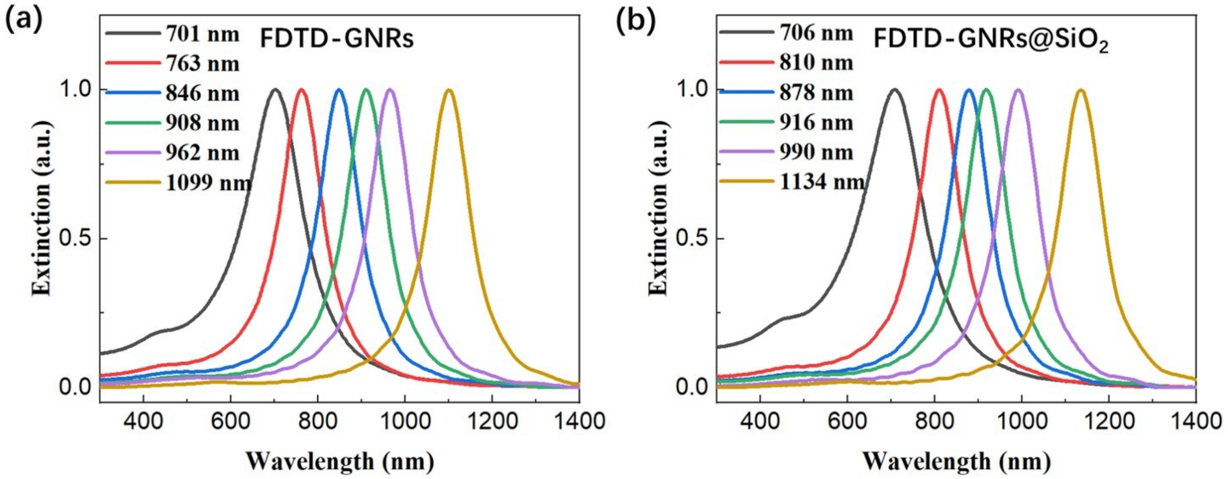

Fig. S3 FDTD simulated spectra. (a) FDTD simulated extinction spectra obtained by excitation of six GNRs of different LSPRs along the longitudinal axis. (b) FDTD simulated extinction spectra obtained by excitation of six GNRs@SiO$_2$ of different LSPRs along the longitudinal axis.

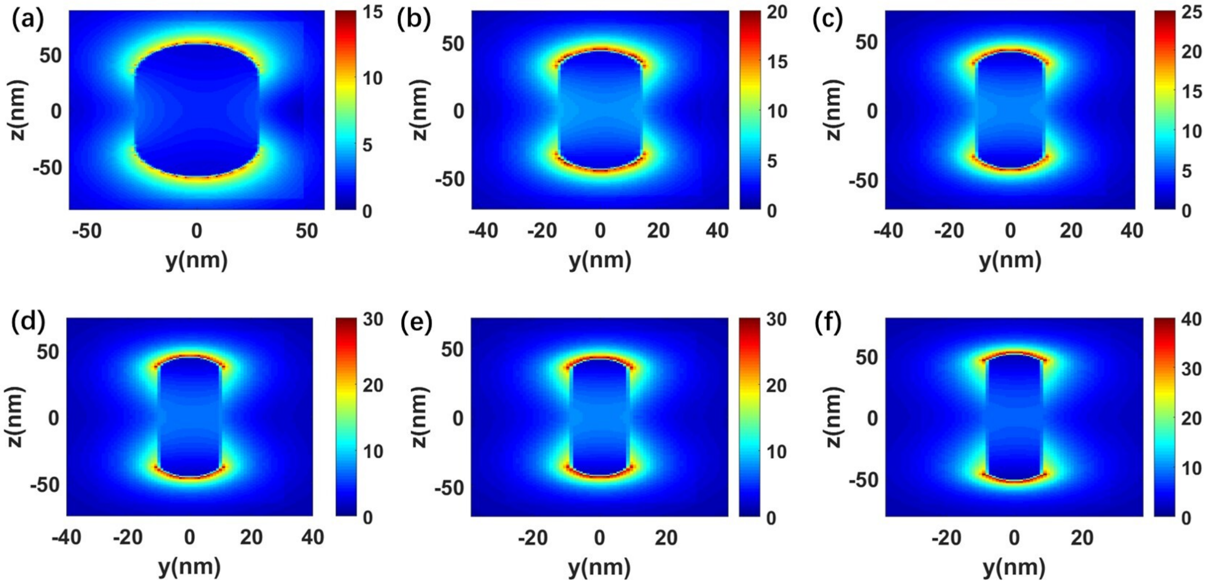

Fig. S4 FDTD simulations of the electric field distribution of single GNRs with different LSPRs, corresponding to Fig. 2a (1-6) of GNRs.

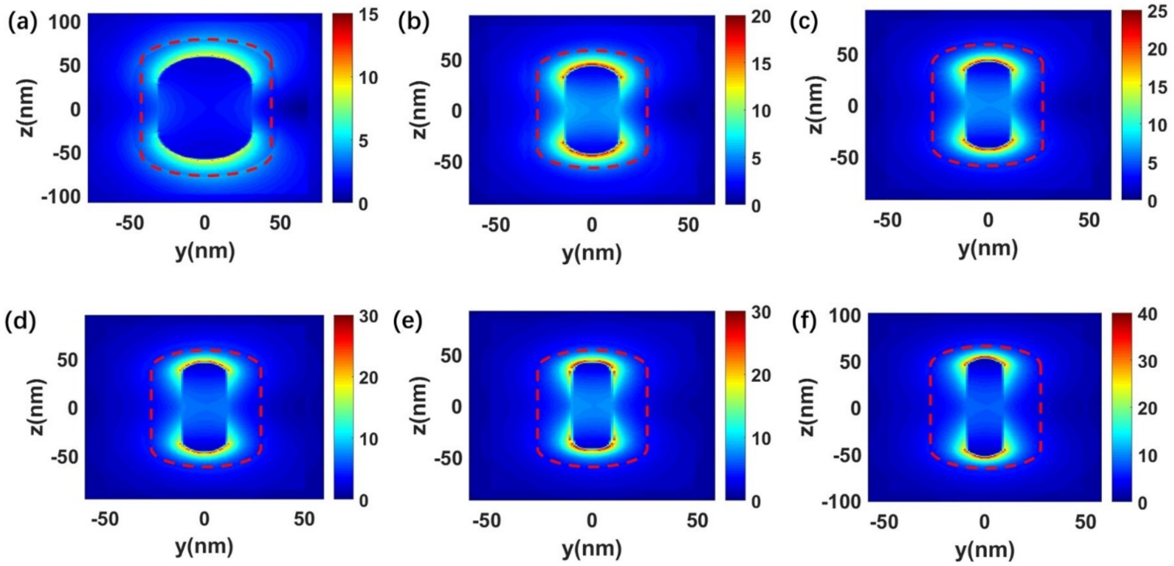

Fig. S5 FDTD simulations of the electric field distribution of a single GNRs@SiO$_2$ with different LSPRs, corresponding to Fig. 2a (1-6) of GNRs@SiO$_2$. There is a layer of mesoporous silica with a thickness of 20 nm on the surface of the GNRs, as shown in the figure between the red dotted line and the GNRs. The electric field outside the red dotted line is very weak.

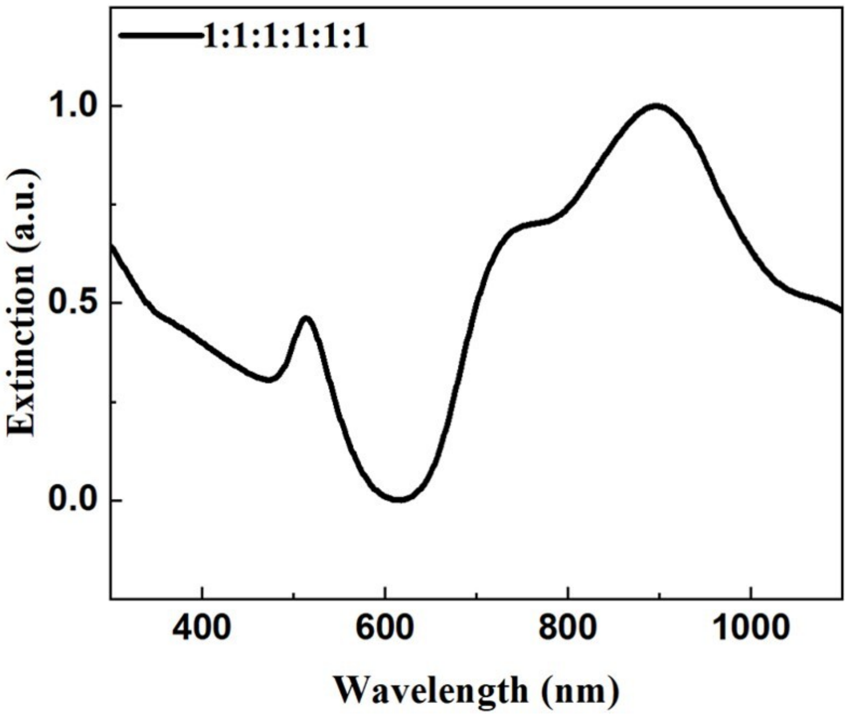

Fig. S6 The calculated spectrum of the mixed solution by the ratio of 1:1:1:1:1:1.

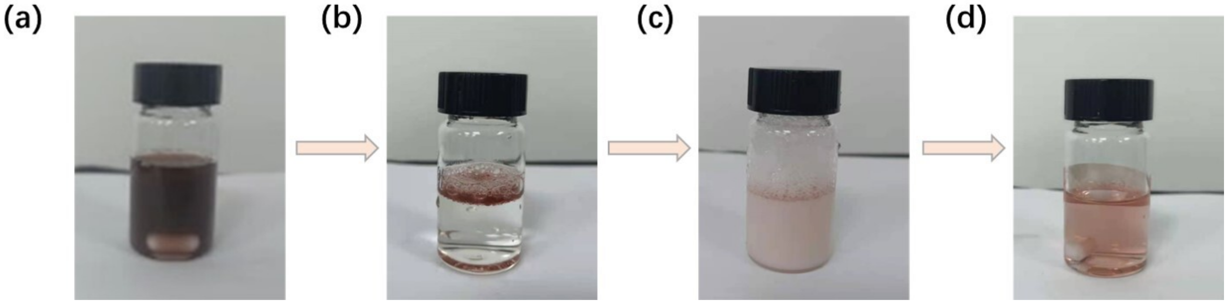

Fig. S7 Photographs of the main steps in the process of self-assembling GNRs@SiO_2 particles into superparticles. (a) The mixed GNRs@SiO_2 dispersed in ethanol solution. (b) The oil-water layered interface is made with GNRs@SiO_2@OTMS particles dispersed in cyclohexane in the upper layer and deionized water in the lower layer. (c) The emulsion obtained after sonication. (d) The broadband superparticles obtained after evaporation of cyclohexane.

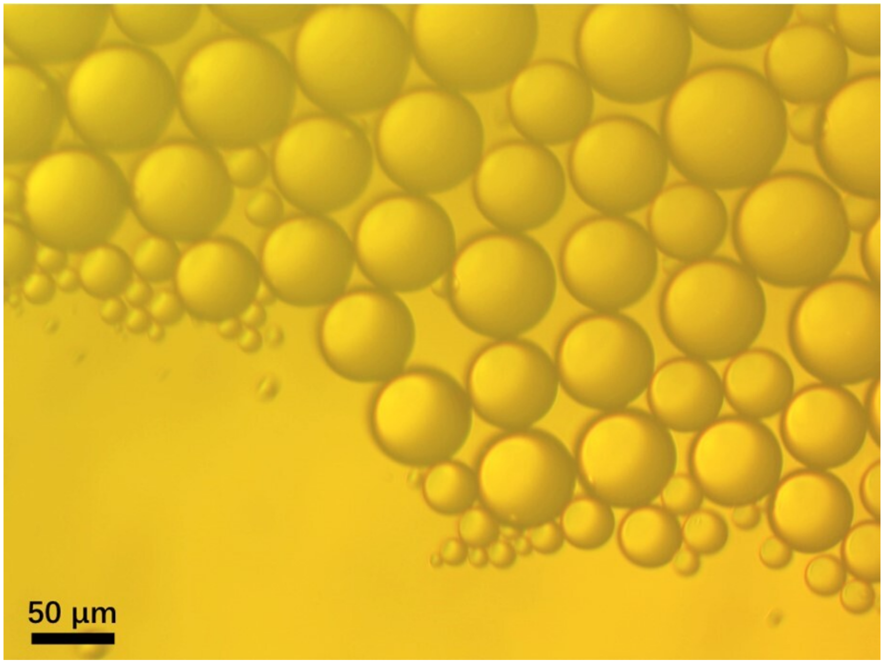

Fig. S8 The cyclohexane oil droplets in the emulsion photographed under an optical microscope with a 10x objective.

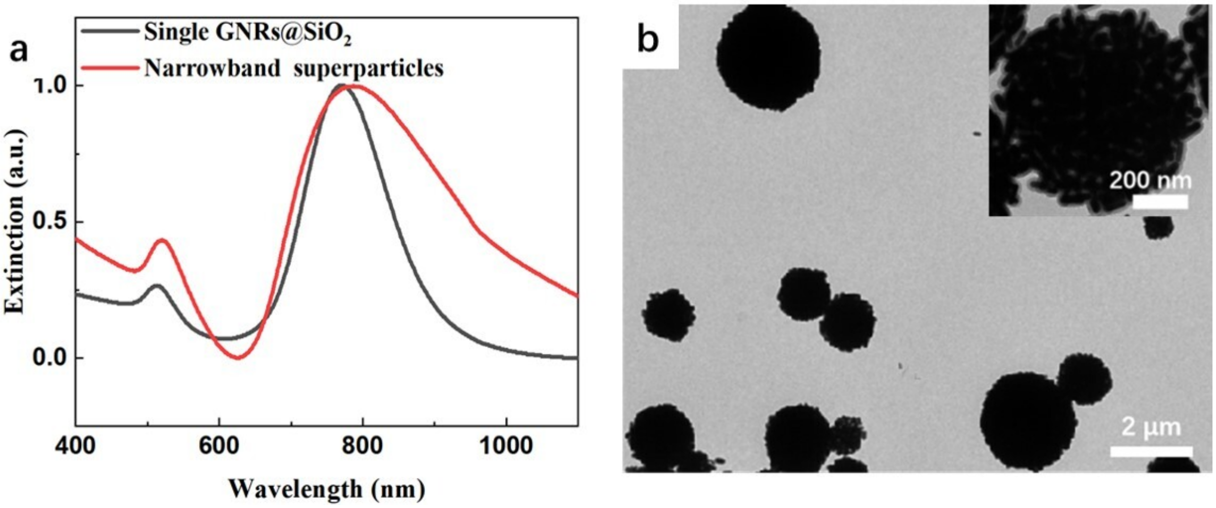

Fig. S9 Extinction spectroscopy and TEM characterization. (a) Extinction spectroscopy of single GNRs@SiO_2 (black, LSPR at 760 nm) and their corresponding superparticles (red). (b) TEM images of narrowband superparticles with average size 1.1 μm.

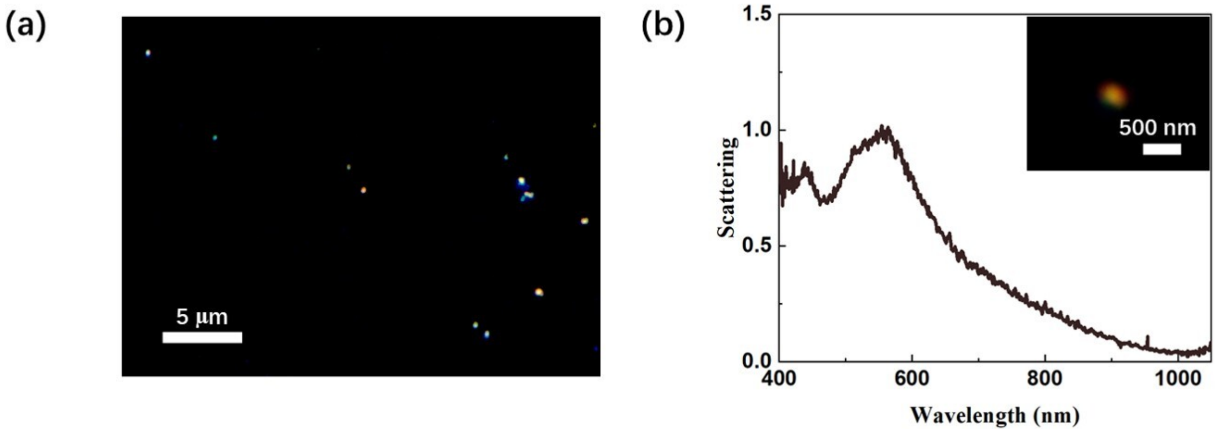

Fig. S10 GNRs@SiO_2 picture in darkfield mode and its corresponding single-particle scattering spectrum. (a) Fig. 2a1 of the GNRs@SiO_2 were prepared on a silicon wafer after dilution of 1000 times, followed by photographs taken with an Olympus BX53M optical microscope with the objective (100×, NA= 0.80). (b) The darkfield single-particle scattering spectrum of the GNRs@SiO_2, and the inset is the picture of corresponding particle taken under dark field condition.

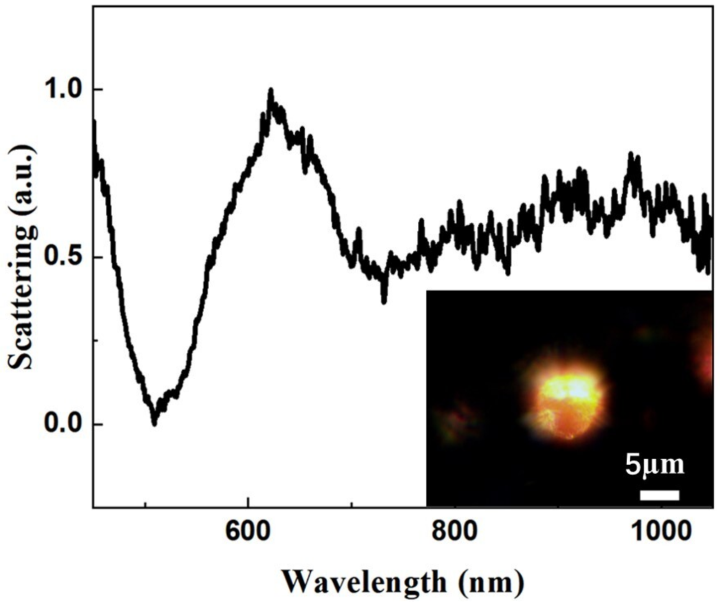

Fig. S11 Darkfield single-particle scattering spectra of broadband superparticles and corresponding photographs. The photograph was taken with an Olympus BX53M optical microscope with the objective (100×, NA= 0.80).

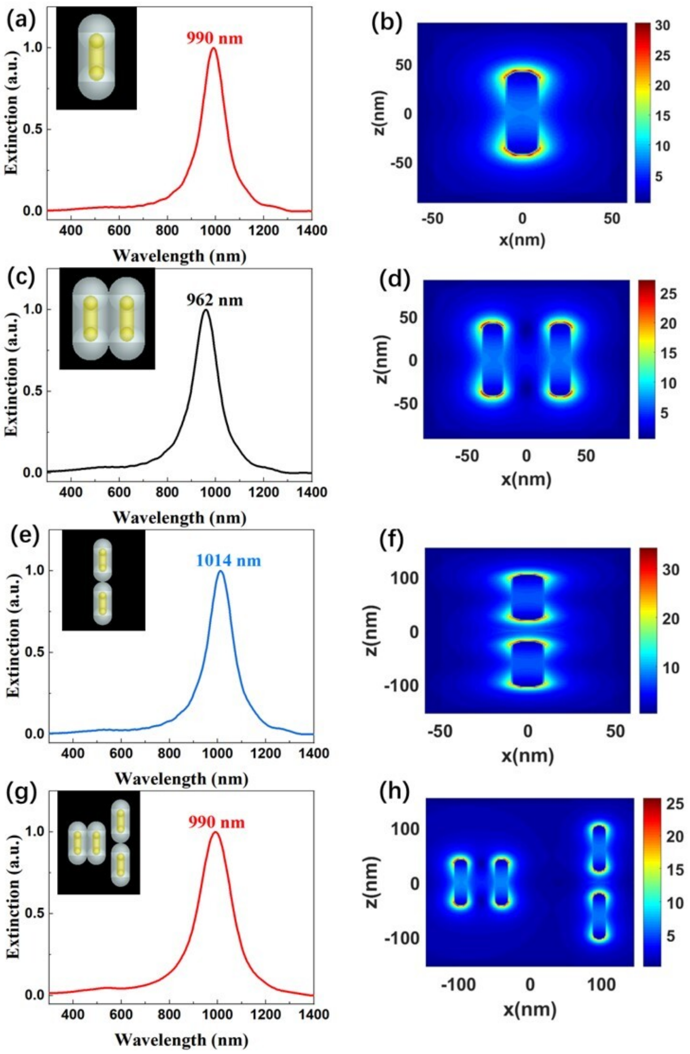

Fig. S12 The extinction spectra and electric field distributions obtained by FDTD simulations illustrate that the plasmonic coupling effect between the GNRs@SiO$_2$ can be ignored. (a, b) extinction spectra (a) and electric field distribution (b) of the GNRs@SiO$_2$ with the LSPR of 990 nm in Fig. S2b. (c, d) (c) is two GNRs@SiO$_2$ of the same size as the model in (a) arranged side-by-side and (d) is the corresponding electric field distribution. (e, f) (e) is two GNRs@SiO$_2$ of the same size as the model in (a) arranged head-to-head and (f) is the corresponding electric field distribution. (g, h) (g) is the GNRs@SiO$_2$ arranged side-by-side and head-to-head together, the peak position is similar to (a), and (h) is the electric field distribution.

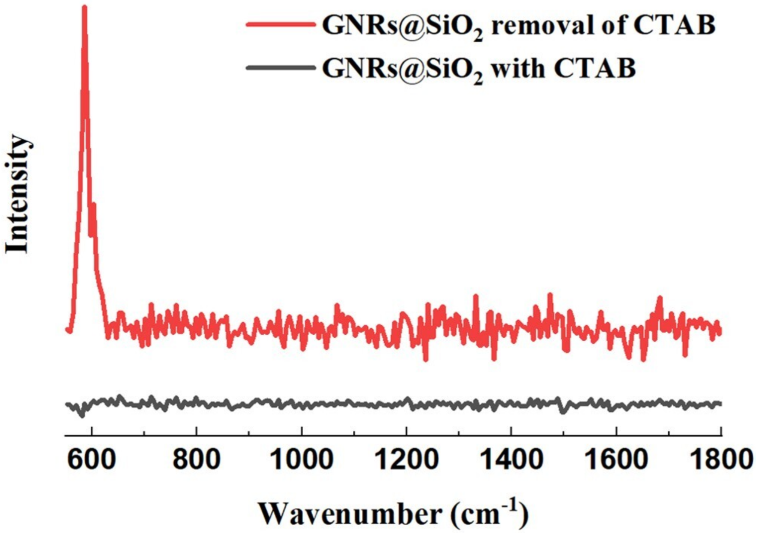

Fig. S13 Effect of removal of CTAB template on SERS performance of GNRs@SiO$_2$. The Raman measurements were recorded with a 785 nm laser, 200 mW laser power, 50 x air objective (NA= 0.75), 10 s exposure time and 1 accumulation per spot.

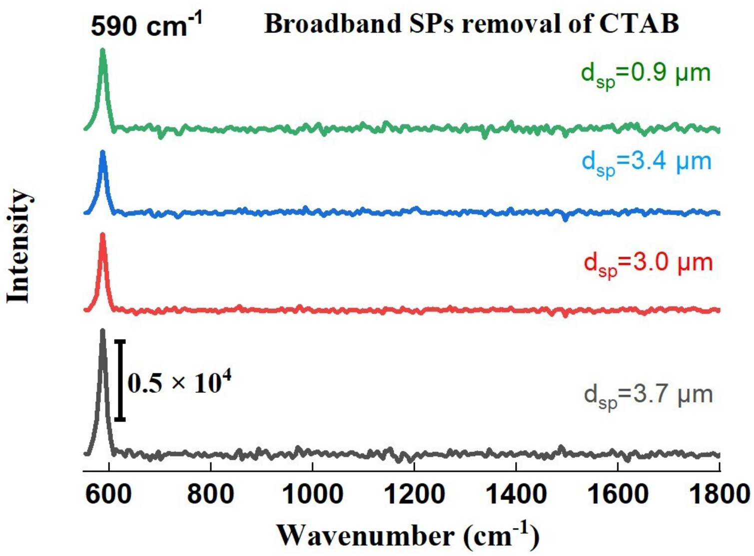

Fig. S14 SERS performance of different sizes of the GNRs@SiO_2 superparticles. The Raman measurements were recorded with a 785 nm laser, 200 mW laser power, 50 x air objective (NA= 0.75), 10 s exposure time and 1 accumulation per spot.

Table S1. Preparation parameters of 6 different sizes of GNRs and related data of measured sizes. The concentrations of $AgNO_3$, $HAuCl_4$, HCl, and AA solutions were 4 mM, 0.01 M, 12.1 M, 0.064 M.

CTAB (g)	NaOL (g)	$AgNO_3$ (mL)	$HAuCl_4$ (mL)	HCl (mL)	AA (mL)	Seed (mL)	Average length (nm)	Average diameter (nm)	Average AR	Fig. number
7.0	1.23	12.0	25.0	2.1	1.25	0.8	117.5±6.4	56.3±2.6	2.1±0.2	Fig. 2a1
7.0	1.23	24.0	25.0	1.5	1.25	0.4	86.8±8.3	28.2±2.0	3.1±0.4	Fig. 2a2
9.0	1.23	24.0	25.0	1.5	1.25	0.1	84.1±14.0	21.4±3.8	3.9±0.4	Fig. 2a3
9.0	1.23	24.0	25.0	2.1	1.25	0.1	90.1±5.4	20.5±1.5	4.4±0.5	Fig. 2a4
7.0	1.23	24.0	25.0	3.6	1.25	0.8	84.0±17.6	17.0±1.0	4.9±1.1	Fig. 2a5
7.0	1.23	24.0	25.0	5.4	1.25	0.8	103.0±13.3	15.7±1.8	6.6±0.9	Fig. 2a6